CAMBRIDGE
UNIVERSITY PRESS

Article

Influence of crystal shape and orientation on the magnetic microstructure of bullet-shaped magnetosomes synthesized by magnetotactic bacteria

András Kovács[1] , Mihály Pósfai[2,3] , Benjamin Zingsem[1], Zi-An Li[4] , Péter Pekker[2], Jan Caron[1] ,
Sandra Prévéral[5] , Christopher T. Lefèvre[5] , Dennis A. Bazylinski[6], Richard B. Frankel[7] and
Rafal E. Dunin-Borkowski[1]

[1]Ernst Ruska-Centre for Microscopy and Spectroscopy with Electrons, Forschungszentrum Jülich, 52425 Jülich, Germany; [2]Research Institute of Biomolecular and Chemical Engineering, University of Pannonia, 8200 Veszprém, Hungary; [3]HUN-REN–PE Environmental Mineralogy Research Group, 8200 Veszprém, Hungary; [4]State Key Laboratory of Featured Metal Materials and Life-cycle Safety for Composite Structures, and School of Physical Science and Technology, Guangxi University, Nanning 530004, China; [5]Aix-Marseille Université, CEA, CNRS, Institute of Biosciences and Biotechnologies of Aix-Marseille, Saint-Paul-lez-Durance, France; [6]School of Life Sciences, University of Nevada at Las Vegas, Las Vegas, Nevada, USA and [7]Department of Physics, California Polytechnic State University, San Luis Obispo, California, USA

Abstract

Cells of magnetotactic bacteria are used as model systems for studying the magnetic properties of ferrimagnetic nanocrystals. Each individual bacterial strain produces magnetosomes (membrane-bounded magnetic crystals) that have distinct sizes, shapes, crystallographic orientations and spatial arrangements, thereby providing nanoparticle systems whose unique magnetic properties are unmatched by synthetic chemically-produced crystals. Here, we use off-axis electron holography in the transmission electron microscope to study the magnetic properties of isolated and closely-spaced bullet-shaped magnetite (Fe_3O_4) magnetosomes biomineralized by the following magnetotactic bacterial strains: the cultured *Desulfovibrio magneticus* RS-1 and the uncultured strains LO-1 and HSMV-1. These bacteria biomineralize magnetite crystals whose crystallographic axes of elongation are parallel to <100> (RS-1 and LO-1) or <110> (HSMV-1). We show that the individual magnetosome crystals are single magnetic domains and measure their projected in-plane magnetization distributions and magnetic dipole moments. We use analytical modelling to assess the interplay between shape anisotropy and the magnetically preferred <111> magneto-crystalline easy axis of magnetite.

Keywords: magnetotactic bacteria; magnetite; transmission electron microscopy; magnetism; off-axis electron holography

(Received 09 November 2023; revised 04 February 2024; manuscript accepted: 04 March 2024)

Introduction

Magnetotactic bacteria (MTB) biomineralize magnetosomes, which are membrane-bounded magnetic iron oxide (magnetite, Fe_3O_4) or iron sulphide (greigite, Fe_3S_4) nanoparticles intracellularly (within their cells) (Bazylinski and Frankel, 2004; Faivre and Schüler, 2008; Komeili *et al.*, 2012). Typically, in the cell, magnetosomes are arranged in one or more chains and/ or in preferred orientations and provide the cell with a magnetic dipole moment that enables magnetotaxis; *i.e.*, passive orientation and then active swimming of the cell along the geomagnetic field lines of the Earth (Frankel *et al.*, 1997). This magnetic sensing mechanism is thought to aid the bacteria in locating and maintaining their optimal positions in vertical chemical concentration gradients (usually O_2 gradients) that occur in their habitats. Each individual bacterial strain biomineralizes magnetic nanoparticles that have specific sizes, shapes and arrangements. By studying the magnetic behaviour of magnetosomes in appropriately chosen strains, competing effects that influence the magnetic dipole moments and magnetic microstructures of individual nanoparticles and their assemblages can be assessed and understood. The influence of nanoparticle size on magnetic domain character, the influence of shape and magneto-crystalline anisotropy on the direction of the magnetic induction within, between and surrounding the particles, the changes that are imposed on the magnetic behaviour of the particles by their interactions and the effects of structural imperfections on local magnetic properties can all be studied.

Cells of MTB have been used as natural nanoscale laboratories for the development and testing of novel magnetic imaging techniques (Dunin-Borkowski *et al.*, 1998; Lam *et al.*, 2010; Le Sage
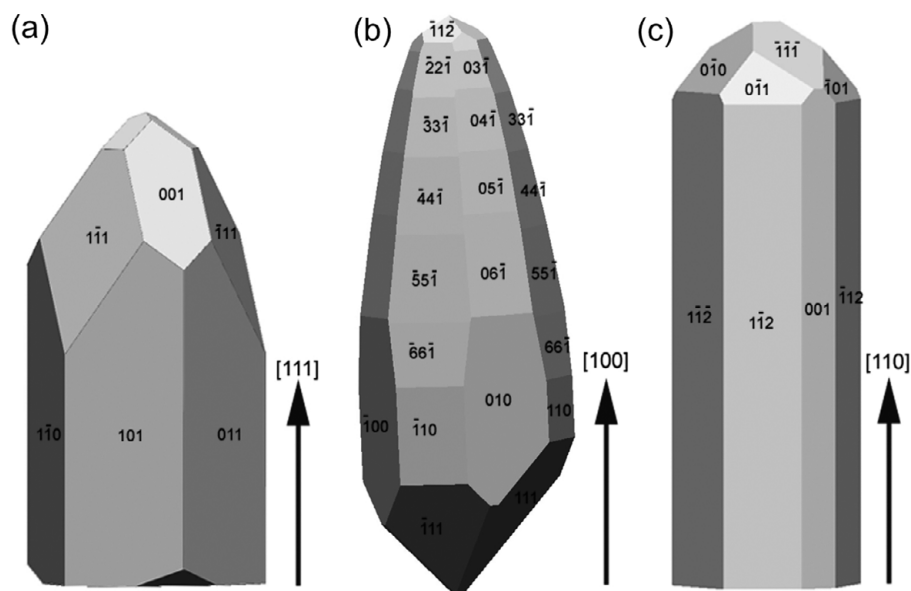
Figure 1. Tentative morphological models of bullet-shaped magnetite magnetosome crystals, whose elongation axes are parallel to (a) <111>, (b) <100> (as in strains RS-1 and LO-1) and (c) <110> (as in strain HSMV-1). The magnetic properties of <111>-elongated magnetosomes from an unidentified strain were described earlier (Pósfai *et al.,* 2013a), while those of <100>- and <110>-elongated crystals from strains LO-1 and HSMV-1, respectively, are the focus of the present study. The models in (b) and (c) are adapted from Lefèvre *et al.,* (2011b).

et al., 2013; Proksch *et al.*, 1995; Staniland *et al.*, 2007) and have been proposed for applications such as genetically engineered magnonic devices (Zingsem *et al.*, 2019). Off-axis electron holography (EH) is a transmission electron microscopy transmission electron microscopy (TEM) method (Kovács and Dunin-Borkowski, 2018) that can provide images of the magnetic microstructures and quantitative measurements of the magnetic dipole moments of magnetosomes with the highest spatial resolution available to date (Pósfai and Dunin-Borkowski, 2009; Pósfai *et al.*, 2013a).

In terms of both magnetism and crystal growth, one of the most intriguing aspects of the properties of magnetosomes is their well-defined, highly constrained and, in many cases, unusual crystal morphology. In general, three basic types of magnetosome habits have been described: cuboctahedral, elongated prismatic and highly elongated bullet-shaped (Pósfai *et al.*, 2013b). With regard to the relationship between crystallography and magnetism, there are two primary possibilities in magnetite-producing MTBs: (i) the <111> magnetocrystalline easy axis is parallel to the chain axis and (ii) a magnetocrystalline hard axis is parallel to the chain axis. These two scenarios are regarded as having cooperative and competitive anisotropy, respectively (Charilaou, 2017).

EH observations of the magnetic behaviours of magnetite magnetosomes with cuboctahedral (Dunin-Borkowski *et al.*, 1998; Dunin-Borkowski *et al.*, 2001 and <111>-elongated prismatic (McCartney *et al.*, 2001; Simpson *et al.*, 2005) shapes in spirilla and cocci, respectively, are consistent with expectations, showing that the direction of magnetic induction within the studied magnetite particles was typically parallel to the <111> easy axis. However, since the <111> crystallographic direction coincides with both the morphological elongation axis of the magnetosome crystals and the chain axis in all known bacterial strains that produce prismatic magnetosomes, previous EH measurements have provided relatively little information about the competing effects of magnetic anisotropies associated with particle shapes and their crystallographic orientations.

Bullet-shaped magnetosome magnetite crystals provide the largest known deviations from the equilibrium morphologies of magnetite crystals. In addition, their morphological elongation axes do

not necessarily coincide with the crystallographic <111> direction. Strains with magnetosome elongation directions parallel to <100> (Byrne *et al.*, 2010; Li, *et al.*, 2015; Li *et al.*, 2010; Pósfai *et al.*, 2006), <110> (Lefèvre *et al.*, 2011b) and <112> (Mann *et al.*, 1987) have been described (Fig. 1), although some of these identifications remain tentative. A list of magnetosome elongation directions in different MTB strains is given in Table 1 (Pósfai *et al.*, 2013b).

The magnetic properties of individual bullet-shaped magnetosomes have not previously been studied in depth. EH has been used in combination with electron tomography to analyze the magnetic induction of a single chain of bullet-shaped, <111>-elongated magnetite magnetosomes in an uncultivated MTB from the River Seine in Paris (Pósfai *et al.*, 2013a). In the latter work, the magnetic induction was found to be parallel to the elongation axes of the individual magnetosomes. For <100>-elongated magnetite magnetosomes, EH data are available from a small number of particles in an MTB that produced mostly greigite magnetosomes (Kasama *et al.*, 2006). An experimental magnetic induction map has also been published for the uncultured strain MYR-1, which produces kinked but mostly <100>-elongated bullet-shaped magnetite magnetosomes (Li *et al.*, 2015). In these studies, the magnetic induction was parallel to the elongation axis of each magnetosome instead of the [111] crystallographic easy axis. To the best of our knowledge, the magnetic behaviour of <110>-elongated bullet-shaped magnetosomes has not previously been studied.

Studies of the magnetic properties of magnetosomes not only provide fundamental insight into the magnetism of nanoparticle systems but are necessary to provide an understanding of magnetotaxis and its evolution. According to genomic analyses, MTB are widely dispersed in 16 phyla in the phylogenetic tree of the domain *Bacteria* (Goswami *et al.*, 2022). However, strains that produce bullet-shaped magnetosomes have only been observed in MTB of the phyla *Thermodesulfobacteriota*, *Desulfobacterota*, *Nitrospirota*, *Omnitrophota* and *Elusimicrobiota* (Pósfai *et al.*, 2013b; Goswami *et al.*, 2022; Uzun *et al.*, 2023), all of which are thought to represent ancient lineages of prokaryotes. On the assumption that magnetotaxis evolved by linear descent and not by horizontal gene transfer, the first magnetosomes were probably bullet-shaped (Lefèvre *et al.*, 2013). By understanding the magnetic properties of bullet-shaped

Table 1. Crystallographic elongations and aspect ratios of magnetite magnetosomes in the bacterial strains studied here. The aspect ratios were measured from TEM images. SS-5 was not studied in detail.

Bacterial strain	Crystallographic elongation	Aspect ratio
Desulfovibrio magneticus RS–1	<100>	2.1 ± 0.4
Candidatus Magnetoovum mohavensis LO–1	<100>	2.2 ± 0.6
Candidatus Thermomagnetovibrio paiutensis HSMV–1	<110>	2.5 ± 0.4
Gammaproteobacterium SS–5	<111>	1.2 ± 0.2

magnetosomes, it may, therefore, be possible to obtain information about the evolution of MTB, as well as about any evolutionary benefit/advantage from magnetotaxis that results from producing magnetite crystals with non-equilibrium morphologies.

The present study aims to analyze the magnetic properties of <100>- and <110>-elongated bullet-shaped magnetite magnetosomes and their chains. We combine quantitative magnetic imaging, electron diffraction, electron tomography and high-resolution TEM to obtain information about the structures, orientations and morphologies of chains and individual magnetosomes. We provide high-spatial-resolution and quantitative analyses of the magnetic induction and magnetization of the magnetosomes using both model-based and model-independent approaches. The results are discussed in the context of both nanoparticle magnetism and the biological functions of biomineralized magnetosomes using analytical approaches and micromagnetic modelling.

Experimental

We studied magnetosomes from the following three strains of MTB (Table 1). *Desulfovibrio magneticus* strain RS-1, which is affiliated to phylum *Thermodesulfobacteriota*, is available in pure culture and produces <100>-elongated magnetite nanoparticles (Pósfai *et al.*, 2006; Rahn-Lee *et al.*, 2015; Sakaguchi *et al.*, 2002). The other two strains are uncultivated and belong to the *Nitrospirota* phylum. Cells of the *Candidatus* Magnetoovum mohavensis strain LO-1, collected from sediments taken from Lake Mead, Nevada, contained <100>-elongated bullet-shaped magnetosomes that were arranged in three twisted chains in each cell (Lefèvre *et al.*, 2011a; Lefèvre *et al.*, 2011b). The *Candidatus* Thermomagnetovibrio paiutensis strain, HSMV-1, is a moderately thermophilic vibrio that was collected from thermal springs in northern Nevada (Lefèvre *et al.*, 2010; Lefèvre *et al.*, 2011b) and contained <110>-elongated magnetosomes that are arranged in a single chain in each cell.

Cells of strain RS-1 were cultivated in a 6 L bioreactor (Labofors 3, Infors, Bottmingen/Switzerland) and grown in a modified version of medium 896, described in the German Collection of Microorganism and Cell Cultures GmbH (DSMZ). Magnetosome purification was performed by using a modified version of the protocol described by Mériaux *et al.* (2015). Late exponential phase cultures ($DO_{600nm} = 1.0$) were harvested by centrifugation (7500 G, 10 min, 4 °C), yielding a pellet of 7.2 g. The cells were resuspended in 40 ml of the purification buffer consisting of 20 mM HEPES ($C_8H_{18}N_2O_4S$, pH 7.5), 0.9% NaCl, 8% glycerol, 1 mM EDTA ($C_{10}H_{16}N_2O_8$) and a protease inhibitor cocktail. The cells were disrupted three times by the use of a French press (1000 PSI, 4 °C) and the magnetosomes were purified magnetically by placing

strong magnets at the bottom of 3×15 ml Falcon tubes containing the suspensions. After 15 h at 4 °C, the magnetosomes had aggregated at the bottom of the tubes (against where the magnets were placed) and the supernate (soluble fraction) was carefully removed. The magnetosome pellets were pooled and resuspended in 2 ml of purification buffer without EDTA, then magnetic separation (2–3 h at 4 °C) was repeated five times in 2 ml Eppendorf tubes. The magnetosomes were finally resuspended in 200 µl of 20 mM HEPES (pH 7.5) and 8% glycerol, flash-frozen in liquid nitrogen and stored at -80 °C. The purified magnetosomes were deposited onto TEM grids. For strains LO-1 and HSMV-1, magnetically concentrated and purified cells from environmental samples were deposited directly on C-coated TEM grids and air-dried. In this way, the original arrangements of magnetosomes in chains within cells of LO-1 and HSMV-1 were mostly preserved. By contrast, different arrangements of magnetosomes from strain RS-1 on TEM grids are likely to have resulted from the self-organization of the nanoparticles and, therefore, do not represent the original spatial relationships within the cells.

Bright-field (BF) TEM images, high-angle annular dark-field (HAADF) scanning TEM (STEM) images and energy dispersive X-ray spectroscopy (EDXS) compositional maps (not shown here) were recorded using an electron probe-aberration-corrected FEI Titan ChemiSTEM instrument operated at 200 kV. For tomographic reconstruction, a series of BF and HAADF STEM images were recorded every 2° over a sample tilt range of ±64° using a single tilt Fischione analytical tomography holder in a ThermoFisher Scientific (TFS) Spectra instrument operated at 300 kV. Image alignment and visualization were performed using TFS Inspect3D and Avizo software. Off-axis EH experiments were carried out in aberration-corrected Lorentz mode in an FEI Titan 60-300 TEM, operated at 300 kV using a Fischione dual-axis tomography TEM specimen holder. The biprism voltage used for off-axis EH was typically ~150 V, resulting in a holographic interference fringe spacing of ~2.5 nm and interference fringe contrast in vacuum of ~20%. Electron holograms were recorded on a 2k × 2k CCD camera and processed using computer scripts written in the Semper image processing language (Saxton *et al.*, 1979), MATLAB and Python-based software. The magnetic contribution to the phase shift measured using EH was separated from the mean inner potential contribution to the phase by taking differences between the phases of pairs of holograms, between which the magnetization direction in the specimen was reversed *in situ* in the TEM by tilting the sample to ±75° and switching on the ~1.5 T magnetic field of the conventional microscope objective lens before returning to magnetic-field-free conditions and tilting the sample back to 0° for EH acquisition (Dunin-Borkowski *et al.*, 1998). Care was taken to ensure that the magnetization direction in the sample reversed precisely and that the diffracting conditions of the crystals did not change in each pair of holograms.

Results

The morphologies of the magnetosome magnetite crystals in strains LO-1 and HSMV-1 were determined from BF TEM images of particles recorded at different specimen tilt angles, resulting in tentative morphological models (Lefèvre *et al.*, 2011b). Although these models are based on combinations of cubic crystal forms (Fig. 1), the outlines of the particles suggest that the elongated crystals are bounded by irregular, curved surfaces parallel to their elongation directions. The 'base' of each crystal in RS-1 and LO-1 is,

however, usually faceted with clearly-developed octahedral {111} faces, as shown in Fig. 1(b). In HSMV-1, the base of each bullet-shaped magnetosome crystal appears to be irregular and perpendicular to the long axis of the crystal, as shown in Fig. 1(c). In each strain, many of the crystals are bent. This feature is not accounted for in the models shown in Fig. 1. A two-step growth process has been suggested for similar bullet-shaped magnetite magnetosome crystals in strain MYR-1, involving the initial formation of a cuboctahedral nucleus followed by anisotropic growth along [100] (Li *et al.*, 2015).

Figure 2 shows results taken from an analysis of the structural characteristics of magnetosome crystals from strain RS-1. The magnetosomes are either scattered or self-organized on the TEM grid in linear chains or ring-like arrangements. The TEM images revealed amorphous shell contrast around each crystal (Figs 2(a), 2(b) and 2(d)), which may be part of the membrane that remained after the magnetosomes were extracted from their cells. However, dedicated experiments would be required to confirm the unambiguous presence of a membrane. Atomic-resolution HAADF STEM images shown in Figs 2(b) and 2(c) reveal a defect-free magnetite structure. The inset digital diffractogram shown in Fig. 2(b) confirms the <100> elongation of the crystal. The degree of elongation of the RS-1 crystals was characterized by an aspect ratio defined as their length divided by their width. By measuring 40 crystals, the average aspect ratio for RS-1 was found to be 2.1 ± 0.4. Information about the three-dimensional shapes of the magnetosome crystals was obtained from tilt series of BF and HAADF STEM images using tomographic reconstruction. Figure 2(d) shows a snapshot of magnetosomes that are arranged in the form of a ring and a corresponding three-dimensional reconstruction, Fig. 2(e), which reveals the shapes and facets of the crystals.

The magnetic states and magnetic stray field distributions of the magnetite magnetosomes were studied using EH. Figures 3(a) and 3(b) show a BF TEM image and corresponding magnetic characterization of a chain of <100>-elongated magnetosome crystals from strain RS-1. The magnetic induction map was produced from the magnetic phase shift image by adding contour lines and colours. To a first approximation, each magnetosome can be seen to contain a single magnetic domain. The magnetic field lines are mostly parallel to both the elongation direction of each crystal and the chain axis. An exception is the second crystal from the lower end of the chain. Its elongation axis is misaligned with respect to the overall chain direction, resulting in curvature of the magnetic field lines within it due to the competing effects of shape anisotropy and magnetostatic interactions with its neighbours. As a result, the magnetic field lines are oriented diagonally in the last crystal. The magnetic contribution to the phase shift across one of the magnetosomes (second from the top in Fig. 3(b)) was analyzed further. Based on a line scan measurement (see Supplementary Material), the step in magnetic phase shift across this crystal was measured to be ~0.26 radians, which is approximately 75% of the phase shift that one would expect for a pure magnetite sphere of the same volume (Dunin-Borkowski *et al.*, 2004). It should be noted that the preparation process and shrinkage of the bacteria during drying can alter the proximity of the grains and hence their interactions when compared to hydrated bacteria in their natural environment.

In an intact MTB cell of strain LO-1, the <100>-elongated magnetosomes are typically arranged in a linear chain. A magnetic induction map and a corresponding BF TEM image of magnetosomes in a disordered chain configuration are presented in Fig. 3(c). Analysis of the measured magnetic field lines provides insight into the influence on the magnetic properties of the crystals of their morphologies and positions relative to the chain axis, which is approximately parallel to the direction of the saturating magnetic field. The first three crystals (going downwards from the top) lie partly on top of each other, effectively creating a magnetic state similar to a horseshoe magnet that results in a deviation of the magnetic induction from the chain axis. In the next four crystals, whose separation is relatively large, the magnetic induction lines approximately follow the elongation directions of the magnetosomes. The largest crystal (marked with an arrow) has an aspect ratio of 3.2 and an elongation axis that is parallel to the direction of
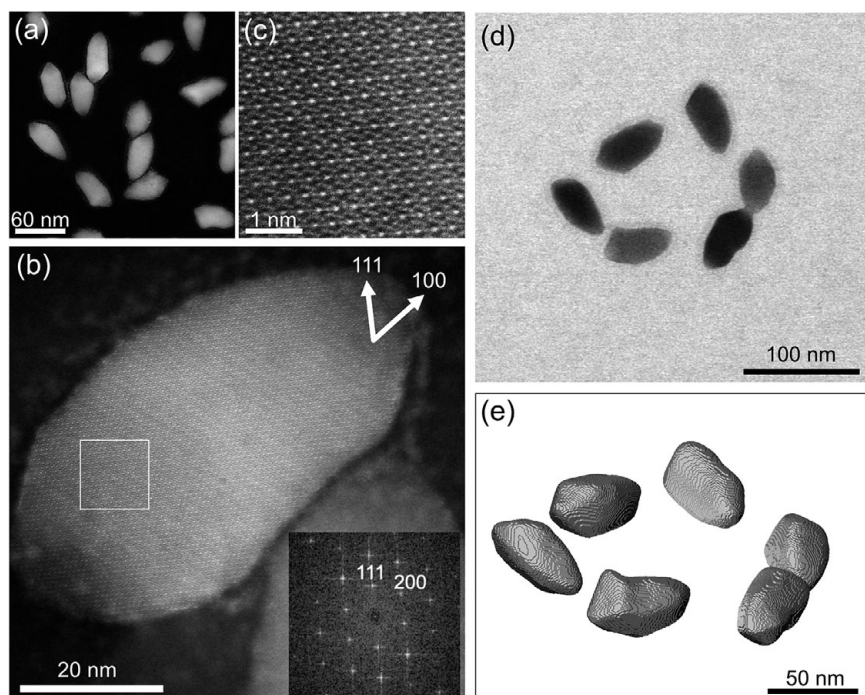

Figure 2. TEM analyses of the structures and morphologies of magnetite magnetosomes extracted from cells of *Desulfovibrio magneticus* strain RS-1: (a) HAADF STEM image of scattered magnetite nanoparticles; (b) High-resolution HAADF STEM image of a single magnetite magnetosome and its digital diffractogram (lower right inset), confirming a perfect magnetite structure and an elongation axis parallel to <100>; (c) Atomic-resolution HAADF STEM image of the magnetite structure; (d) BF STEM image of a ring of magnetite magnetosomes extracted from a tilt series; and (e) Tomographic reconstruction from HAADF STEM images series of the nanoparticle shapes, revealing the presence of facets. A video file is provided as supplementary information.
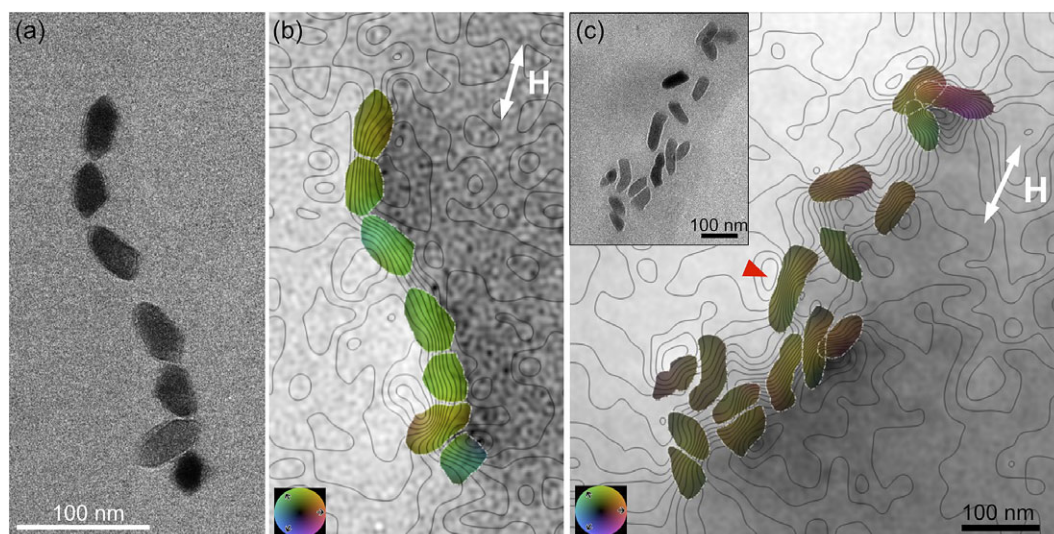
Figure 3. BF TEM images and magnetic induction maps of <100>-elongated magnetosomes from (a, b) strain RS-1 and (c) strain LO-1: (a) BF TEM image of a chain of magnetosomes from strain RS-1; (b) a corresponding magnetic induction map recorded using off-axis EH after saturating the sample magnetically in the direction of the double-headed arrow marked 'H'; and (c) magnetic induction map of a disordered chain of magnetosomes from strain LO-1. The inset shows a BF TEM image of the same crystals. Colours are used to indicate the direction of the projected in-plane magnetic induction, according to the inset colour wheels. The magnetic phase contour spacing in (b) is 0.0375 radians and in (c) 0.054 radians.
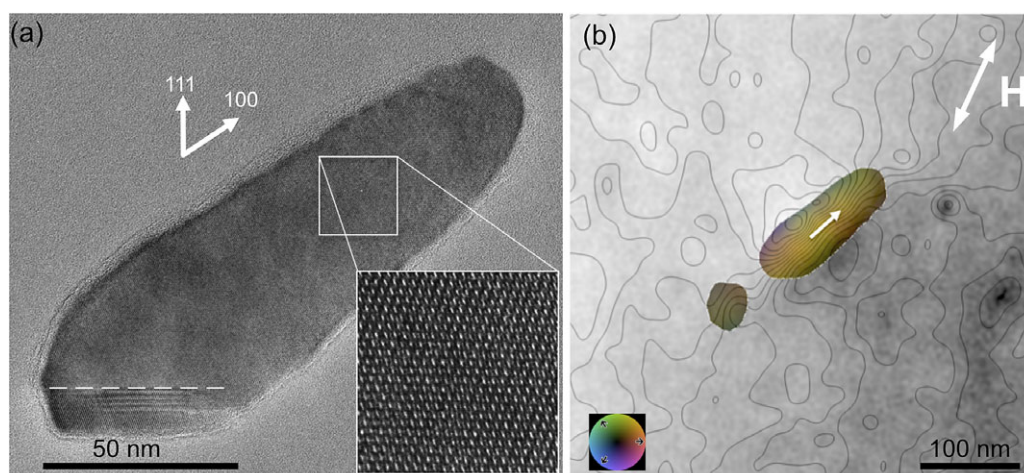

Figure 4. Structural and magnetic characterization of an individual <100>-elongated magnetosome from strain LO-1: (a) high-resolution TEM image recorded along the crystallographic [110] direction of magnetite (the dashed line marks a twin boundary and the inset shows a magnified high-resolution TEM image of the marked region) and (b) a corresponding magnetic induction map. Colours are used to indicate the direction of the projected in-plane magnetic induction, according to the inset colour wheel. The phase contour spacing is 0.06 radians. The double-headed arrow marks the direction of the magnetic field used to saturate the magnetosome.

the saturating field. The magnetic induction lines run approximately parallel to its long axis. They are most closely spaced in the middle of the crystal, increasing their separation at each end as a result of the projection of the in-plane component of the three-dimensional magnetic flux density in the electron beam direction. The remaining nine crystals lie side by side. The magnetic field lines connect many of the crystals to their immediate neighbours as a result of their stray fields and the magnetostatic interactions between them. The average aspect ratio of the magnetosome crystals from cells of strain LO-1 strain is measured to be 2.2 ± 0.6.

An HRTEM image (Fig. 4(a)) and a corresponding magnetic induction map (Fig. 4(b)) were recorded from an individual magnetosome from strain LO-1, whose morphology is similar to the model shown in Fig. 1(b). This crystal has a length of ~145 nm and a width of ~48 nm in its middle section, with an aspect ratio of ~3. It is elongated along <100>, as confirmed by a digital diffractogram (not shown) generated from the atomic-resolution TEM image. The dashed line in Fig. 4(a) marks a twin boundary in the magnetite structure (Devouard *et al.*, 1998). A few-nm-thick amorphous shell, which is visible on the surface of the magnetosome, may represent the remaining membrane material. Such a membrane may protect the crystal from oxidation, making the magnetosome a model system for studying the structure and magnetism of magnetite (Zhu *et al.*, 2015). A magnetic induction map of the magnetosome (Fig. 4(b)) was recorded using off-axis EH after saturating it magnetically in a direction approximately 20° from its long axis. The magnetic field lines in the crystal confirm the presence of a single-domain magnetic state. They do not appear to follow any of the

Figure 5. TEM analysis of the structure and magnetic properties of <110>-elongated magnetosomes from strain HSMV-1: (a) BF TEM images, recorded in magnetic-field-free conditions, with dark image contrast corresponding to a bacterial cell and its magnetosomes; (b) magnetic induction map recorded from the region marked in (a) using off-axis EH (the magnetic phase contours have a spacing of 0.2 radians); (c) BF TEM image; and (d) magnetic induction map of a chain fragment from another cell of strain HSMV-1. The magnetic phase contours have a spacing of 0.1 radians. The double-headed arrows in (b) and (d) indicate the direction of the magnetic field used to saturate the magnetosomes. The scale bars are 100 nm.
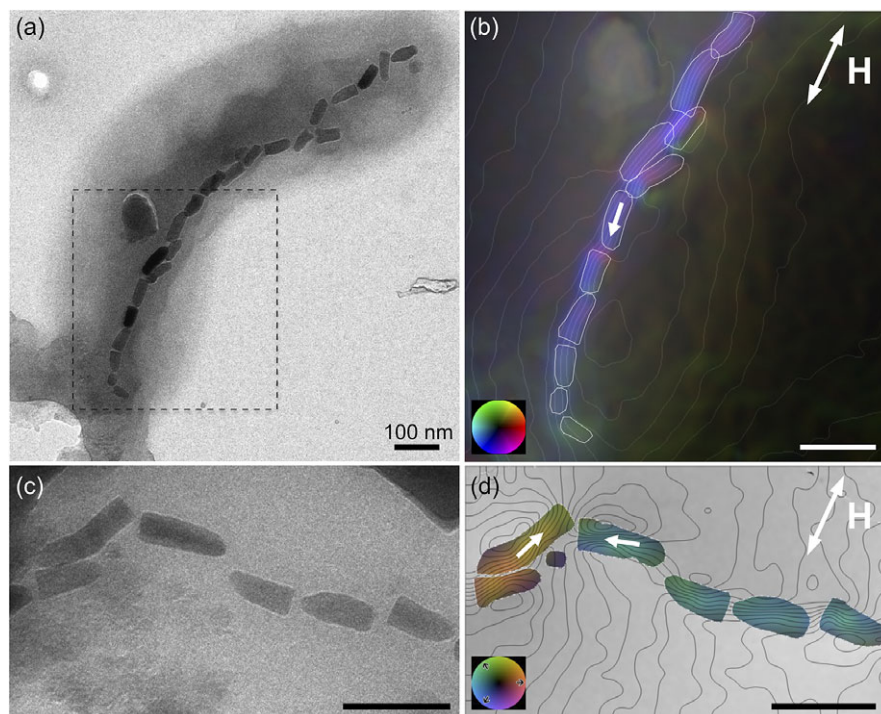
<111> magnetic easy axis directions, which are oriented approximately 55º from the long axis of the magnetosome. The magnetic induction lines seem to form a bundle inside the crystal and are more widely spaced near its surface and ends, suggesting the presence of a three-dimensional magnetic state. The minimum-energy magnetic configuration of an elongated nanoparticle can be described as a flower or twisted flower state close to its ends, based on finite element micromagnetic simulations (Fabian *et al.*, 1996; Hertel and Kronmüller, 2002). The step in the magnetic phase shift across the middle of the magnetosome, where the magnetic field lines are most closely spaced and approximately parallel to its elongation direction, is measured to be 0.72 radians, which is slightly smaller than the value of 0.78 radians expected for a uniformly-magnetized 48-nm-diameter magnetite crystal.

Figures 5(a) and 5(b) show a BF TEM image and the corresponding magnetic field distribution of <110>-elongated magnetosomes from strain HSMV-1, which are preserved inside a dried cell. Dark contrast around the chain in the BF TEM image is associated with the remains of the dehydrated bacterial cell, whose presence is likely to have contributed to the preservation of the magnetosomes in the form of a linear chain. Some of the crystals are bent or kinked (similar to those described by Hanzlik *et al.* (2002)). The average aspect ratio of the magnetosome crystals is measured to be 2.5 ± 0.4 (*c.f.* RS-1 = 2.1; LO-1 = 2.2). A magnetic induction map recorded from the lower part of the chain is presented in Fig. 5(b). The magnetic field is confined to be parallel to the elongation direction of each particle, which coincides closely with the chain axis. The magnetic induction does not change significantly between the magnetosomes as the gaps between adjacent crystals are small compared to their lengths. In some cases, the magnetosomes overlap in projection. The step in the magnetic contribution to the phase shift across the <110>-elongated magnetosomes in a direction perpendicular to the chain axis was measured to be approximately (1 ± 0.2) radians, which is in the same range as that predicted for a spherical 50–60 nm magnetite crystal. As the magnetic phase shift

increases rapidly from 0.63 to 1.52 radians for particles with sizes of 45 to 70 nm, errors in measurements of particle size can have a significant effect on magnetic quantification.

Figures 5(c) and 5(d) show a BF TEM image and a corresponding magnetic induction map of a section of a chain that contains six <110>-elongated magnetosomes. In this arrangement, the long axes of two of the crystals are parallel to the direction of the saturating magnetic field, while the other four crystals are oriented perpendicular to the saturating magnetic field. The two chain sections become magnetized in opposite directions after the application of a saturating field (*H*), although within each section the magnetization directions are parallel to the long axes of the crystals. Magnetosomes with opposing magnetic polarity are a clear artifact resulting from the external magnetic field applied perpendicular to the chain axis. In earlier studies, antiparallel sub-chain polarities were observed in strain MV-1 (Kalirai *et al.*, 2013).

Discussion

Magnetic induction maps have been recorded from bullet-shaped magnetite crystals with <100>, <110> and <111> crystallographic directions of elongation. Results for the first two directions are presented in this study while magnetic induction maps were previously obtained from <111>-elongated magnetosomes (Pósfai *et al.*, 2013a) in which the magnetic induction was also measured to be parallel to the particle elongation axes. Taken together, the results show that the factors that dominate magnetic properties are the elongated shapes of the crystals and magnetostatic interactions between them when they are closely spaced. Similar conclusions were drawn from results obtained using ferromagnetic resonance spectroscopy of bullet-shaped <100>-elongated magnetosome crystals from strain RS-1 (Charilaou *et al.*, 2015), suggesting that shape anisotropy caused by the bullet-shaped morphology compensates for the less optimal alignment of the crystallographic magnetic easy axis. Our direct measurements, recorded from chains
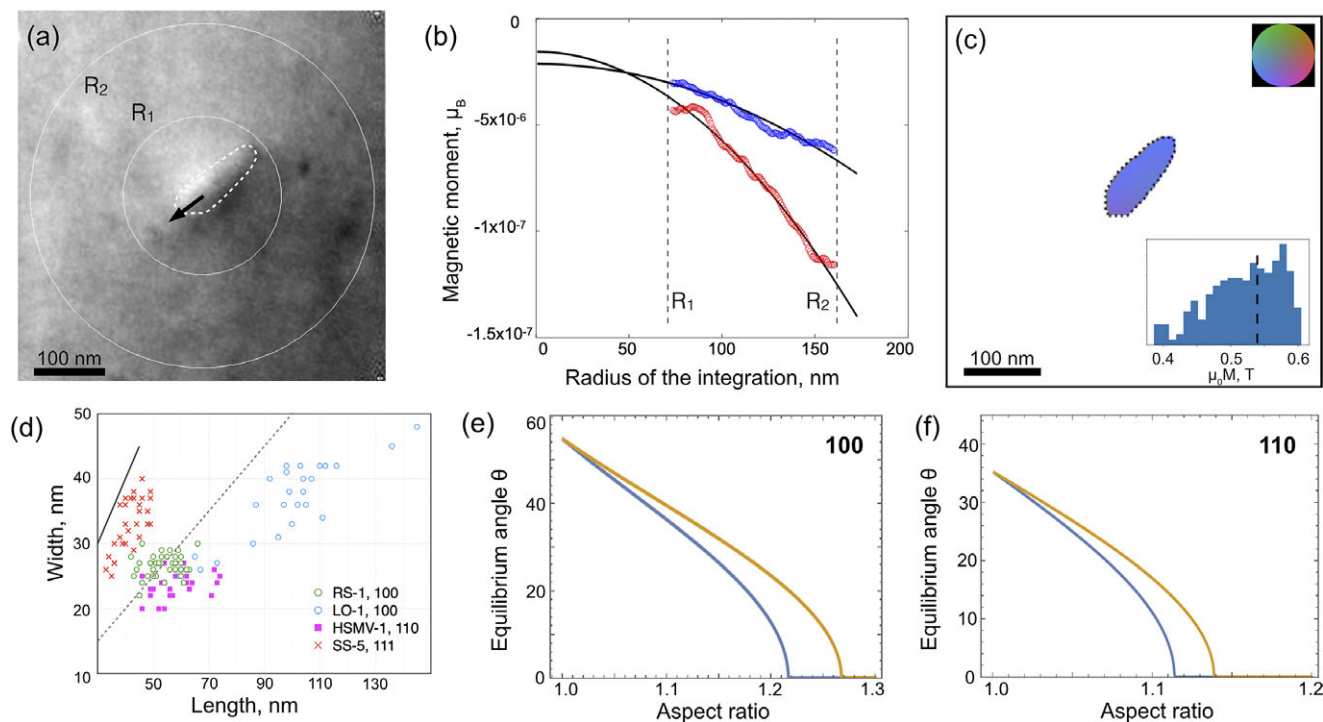
Figure 6. Measurements of magnetic dipole moment and magnetization of the <100>-elongated magnetite crystal shown in Fig. 4: (a) Magnetic phase shift image showing the inner and outer integration boundaries R_1 and R_2, respectively, used for model-independent measurement of the in-plane magnetic dipole moment. (See text for details). The direction of the measured moment is indicated using an arrow; (b) Parabolic fits of the measured inductive magnetic dipole moment (Beleggia *et al.*, 2010); (c) Results of model-based iterative reconstruction of the projected in-plane magnetization distribution in the particle and its histogram (inset); and (d) Measurements of the aspect ratios of magnetosome crystals based on their length and width, providing values of 2.1, 2.2, 2.5 and 1.2 for strains RS-1, LO-1, HSMV-1 and SS-5, respectively. The solid and dashed lines correspond to aspect ratios of 1 and 2, respectively. Figures (e) and (f) show the equilibrium angle of the total magnetic contribution to the Helmholtz free energy density from the particle's long axis to the nearest magnetocrystalline easy axis as a function of aspect ratio for <100> and <110> elongations, respectively. The blue and orange curves correspond to pure magnetite and a slightly oxidized structure, respectively.

and individual magnetosomes, provide deeper insight into the role of elongation and the persistence of the bullet-shaped magnetosome crystal morphology.

We used experimental magnetic phase shift images to record magnetic induction maps from <100>- and <110>- elongated bullet-shaped magnetosomes extracted from MTB strains RS-1, LO-1 and HSMV-1. The phase shift images can be used to provide quantitative magnetic information about individual crystals. For an individual <100>-elongated magnetosome from strain LO-1 (Fig. 4), we first used a model-independent approach based on contour integration of the magnetic phase gradient (Beleggia *et al.*, 2010) to determine the in-plane magnetic dipole moment from the phase image. The integration contours were circles of decreasing radius R_2 to R_1, with the smaller circle touching the magnetosome boundary, as shown in Fig. 6(a). The measurements were extrapolated to zero integration radius, as shown in Fig. 6(b), to eliminate systematic sources of error from the measurements. The measured value of the in-plane magnetic dipole moment was 4.07×10^6 μ_B oriented in the direction of the black arrow marked in Fig. 6(a). By estimating the volume of the magnetosome from its dimensions measured from a BF TEM image, the average saturation magnetic induction was inferred to be 0.52 ± 0.04 T, which is slightly smaller than the expected value of 0.6 T for magnetite (Dunlop and Özdemir, 1997). We also measured the projected in-plane magnetization distribution in the magnetosome using model-based iterative reconstruction (Caron, 2017). We previously used this approach to measure the magnetic properties of skyrmions in FeGe (Kovács *et al.*, 2017) and precipitates in a high

entropy alloy (Lan *et al.*, 2022). With this approach, simulated magnetic phase images are calculated based on successive guesses for the projected in-plane magnetization distribution $M(x,y)$ in the analyzed part of the specimen. It makes use of analytical solutions for the phase shifts of simple geometrical objects, with numerical discretization performed in real space to avoid artifacts generated by discretization in Fourier space. The forward simulations are used in an iterative scheme to solve the inverse problem of reconstructing the projected in-plane magnetization distribution in the sample, which can then be converted into values of in-plane magnetization based on a measurement of the sample thickness. Figure 6(c) shows the resulting projected in-plane magnetization map of the magnetosome crystal studied in Fig. 4 and Figs 6(a) and 6(b). The projected in-plane magnetization is approximately uniform, as expected for a single magnetic domain. The inset to Fig. 6(c) shows a histogram of the inferred values of magnetization, whose average is 0.54 ± 0.08 T. Uncertainties about the crystal thickness and surface layer can contribute to both statistical and systematic errors in the inferred magnetization values. The results of the different measurements are summarized in Table 2.

Table 2. Measured morphological and magnetic parameters for the <100>-elongated magnetosome analyzed in Figs 4 and 6

Strain	Size [nm]	Aspect ratio	φ_m [rad]	φ_m(exp.) [rad]	**B** (exp.) [T]	$\mu_0 M$(exp.) [T]
LO–1	145 x 48	3	0.78	0.72±0.06	0.52±0.04	0.54±0.08

Slightly smaller values of magnetic phase shift and magnetization were measured from crystals in all three studied strains than expected for pure magnetite. This deviation may be explained by uncertainties in the size and volume determination of the particles, as well as by partial oxidation from magnetite to maghemite (γ-Fe_2O_3), the latter having a lower value of saturation magnetization (0.48 *vs* 0.6 T).

We now discuss the influence of magnetosome aspect ratio on the interplay between magnetocrystalline and shape anisotropy by following a similar logic to that of Körnig et al. (2014). TEM imaging of the magnetosomes allows the aspect ratios of the crystals to be determined from measurements of their lengths and widths. Values obtained for <100>- and <110>-elongated crystals from strains RS-1, LO-1 and HSMV-1, respectively, are plotted in Fig. 6(d) alongside data from strain SS-5, which produces <111>-elongated magnetite crystals (Lefèvre *et al.*, 2012). The average crystal aspect ratio is measured at 2.1, 2.2, 2.5 and 1.2 for strains RS-1, LO-1, HSMV-1 and SS-5, respectively. This analysis assumes that the aspect ratio does not change with crystal size. The large (>2.0) aspect ratios observed here for strains RS-1, LO-1 and HSMV-1 suggest that the studied magnetosome crystals are well-developed and mature.

By considering the saturation magnetization and magnetic anisotropy constants of magnetite, the total magnetic contribution to the Helmholtz free energy density (F_{total}) can be defined as the sum of magnetocrystalline anisotropy (F_c) and demagnetizing (F_{demag}) energies. By calculating the equilibrium angle of the magnetization (θ) at which F_{total} is minimized, a threshold value for the aspect ratio can be defined, above which the magnetic moments follow the elongation direction of a crystal rather than the magnetocrystalline easy axis (as also found for strain RS-1 by Körnig *et al.*, 2014). Details of the analysis are provided in the Supplementary Material. Figures 6(e) and 6(f) show plots of θ *vs* aspect ratio for <100> and <110> crystal elongations. Our experimental phase shift and magnetization measurements (Figs 3–6) suggest that some magnetic parameters such as saturation magnetization may be reduced slightly when compared with values for ideal magnetite particles. Accordingly, blue and orange curves are plotted in Figs 6(e) and 6(f) for pure magnetite and a slightly oxidized (maghemite) structure, respectively. The threshold values of the aspect ratio for <100> and <110> elongation directions are determined to be in the range of 1.21-1.27 and 1.11-1.14, respectively. These calculations suggest that, from a magnetic perspective, a relatively small amount (~25%) of particle elongation along a magnetic hard axis is sufficient to stabilize the direction of the magnetic dipole moment in a crystal along its elongation axis, in agreement with previous modelling and experimental studies (Körnig *et al.*, 2014; Charilaou *et al.*, 2015; Moreno *et al.*, 2020).

Our analysis of individual and disordered chains of closely-spaced magnetosomes shows that the chain configuration can be the most important factor affecting the direction of magnetic induction within and surrounding the magnetite crystals. Magnetostatic interactions between nanoparticles have been shown to be important in previous analyses of magnetosome chains (Dunin-Borkowski *et al.*, 1998; Dunin-Borkowski *et al.*, 2001; McCartney *et al.*, 2001). The highly elongated shapes and different crystallographic elongation directions analyzed in the present study provide direct evidence that the order of importance in the determination of the magnetic induction direction in closely-spaced magnetosomes is, typically, (1) interparticle interactions, (2) shape anisotropy and (3) magnetocrystalline anisotropy.

The highly elongated shapes of the crystals studied here are likely to be beneficial for the efficiency of magnetic orientation of the bacterial cells, since the distinct particle shapes constrain the magnetic induction to be parallel to their elongation axes, which typically coincide with the chain direction. However, our results do not provide an explanation for why there are (at least) three different crystallographic elongation axes of such crystals, including <100> and <110>, which are less likely to have been selected by evolution than <111>, which lies parallel to the crystallographic magnetic easy axis of magnetite. Our magnetic induction maps show that, if the particles are in chains, then particle shape and elongation do not play the most significant role magnetically since magnetostatic interactions between adjacent magnetosomes can then have the greatest effect on the direction of the magnetic field. Therefore, the evolutionary driving force behind the development of different crystallographic directions in bullet-shaped magnetosomes is unlikely to be associated with the optimization of magnetotaxis, but may instead result from magnetosome gene variations.

The genetic background to the formation of magnetite magnetosomes has been studied extensively over the past 20 years for two model organisms – strains *Magnetospirillum gryphiswaldense* MSR-1 and *Magnetospirillum magneticum* AMB-1 – both of which belong to the *Alphaproteobacteria* class in the *Pseudomonadota* phylum and produce cuboctahedral crystals (Komeili *et al.*, 2012; Lohsse *et al.*, 2014). In these two closely-related strains, it was shown that magnetosome formation is controlled by magnetosome membrane proteins that are encoded by so-called *mam* and *mms* genes, which cluster in a specific chromosomic region that is referred to as the 'magnetosome gene cluster' (MGC). Magnetosome synthesis was shown to be affected in genetically engineered mutants that lacked specific genes or operons in the MGC, with gene deletions resulting in the formation of either smaller or structurally less perfect magnetite crystals when compared to wild-type cells, or in the inability of cells to assemble magnetosomes in chains (Lohsse *et al.*, 2014). On the other hand, the transfer of a minimal set of magnetosome synthesis genes from MSR-1 to non-magnetotactic bacteria resulted in the formation of magnetosome chains in these organisms (Kolinko *et al.*, 2014; Dziuba *et al.*, 2023). Despite this progress in understanding the functions of magnetosome proteins, almost nothing is known about genetic control over crystal morphology since strains MSR-1 and AMB-1 biomineralize cuboctahedral, equant magnetite crystals, whose morphologies approach the equilibrium shape of magnetite and are, therefore, likely to require less morphological control.

As discussed in the Introduction, bullet-shaped magnetosomes are formed in MTB that belong to the *Thermodesulfobacterota*, *Nitrospirota*, *Omnitrophota* and *Elusimicrobiota* phyla clades, which emerged before the *Pseudomonadota* phylum that contains all MTB that produce prismatic and cuboctahedral magnetite crystals. Bullet-shaped magnetite producers are therefore considered to be from more ancient prokaryotic lineages (Lefèvre *et al.*, 2013). When compared to the *Alphaproteobacteria*, less genetic information is available from MTB from *Nitrospirota* (Jogler *et al.*, 2011; Kolinko *et al.*, 2011; Lin *et al.*, 2014), to which two of the strains analyzed in the present study (LO-1 and HSMV-1) belong. In addition to *mam* genes, all MTB that biomineralize bullet-shaped magnetosomes have another specific group of genes in their genomes, which is referred to as *mad* genes. Although little is known about the function of the proteins that are encoded by *mad* genes, it is possible that some of these genes are involved in controlling the shapes and crystallographic orientations of anisotropic magnetite

crystals. The gene *mad10*, found in the MGC of *Desulfamplus magnetovallimortis* (Descamps *et al.*, 2017), is a cultured MTB that can biomineralize both bullet-shaped magnetite and cuboctahedral greigite and has been proposed to be involved in the elongation of anisotropic magnetite (Pohl *et al.*, 2019). This gene is conserved in all MTB that form bullet-shaped magnetite, including the strain RS-1. The genomes of LO-1 and HSMV-1 were not available at the time of writing.

Recent studies have provided conflicting results about magnetite biomineralization in *D. magneticus* strain RS-1 (Baumgartner *et al.*, 2016; Rahn-Lee *et al.*, 2015). This organism possesses a MGC that differs significantly from that in the *Alphaproteobacteria* (Rahn-Lee *et al.*, 2015). Whereas mutants of the magnetotactic *Alphaproteobacteria* typically produce full chains of poorly-developed magnetite crystals, mutants of strain RS-1 synthesize fully-developed but fewer magnetosomes than their wild-type counterpart. It has been suggested that magnetosomes in RS-1 are mineralized one at a time in a 'central magnetosome factory' and that the crystals dissociate into chains from this point of synthesis (Rahn-Lee *et al.*, 2015). Such a magnetosome growth scenario could, perhaps, explain the two-step growth process of bent, bullet-shaped magnetosome magnetite crystals (Hanzlik *et al.*, 2002), as has been suggested for strain MYR-1 (Li *et al.*, 2015; Li *et al.*, 2010). Whereas the nucleation and initial growth of magnetite crystals could take place in a vesicle under strict biological control, thereby producing a euhedral 'base' for the crystal, subsequent growth of the pointed, elongated part could result from an anisotropic flux of Fe as the particle is ejected from the 'magnetosome factory'. A different route to magnetite mineralization in RS-1 has been suggested by Baumgartner *et al.* (2016), who reported that an iron oxyhydroxide precursor, green rust, converts to magnetite in the solid state. However, neither of these crystal growth scenarios provides a satisfactory explanation for the formation of highly specific bullet-shaped crystals or for the occurrence of different crystallographic elongations of magnetite crystals in different magnetotactic strains. Future genomic analyses may provide additional information about magnetosome chain formation to resolve the genetic origins of the different crystallographic elongation directions.

Finally, we briefly speculate here on whether bullet-shaped magnetite magnetosome crystals can be used as reliable biomarkers. Magnetite crystals similar to those produced by MTB have been preserved in the geologic record and have been termed magnetofossils (Petersen *et al.*, 1986; Kopp and Kirschvink, 2008). Since bullet-shaped crystals are considered to be from MTB of ancient evolutionary lineages, as described earlier, their presence in rocks would be indicative of, and therefore a proxy for, the past presence of MTB from these groups. In addition, the presence of these crystals may also provide information about past and present environmental conditions under which they were formed (Yamazaki *et al.* 2019; Li *et al.* 2020). Bullet-shaped magnetite crystals similar to those described here have been found in several different environments, including the chimney of a hydrothermal vent (Nakano *et al.*, 2023), although the interpretation of these findings is not clear. However, some trends have been observed. For example, anisotropic (*e.g.*, bullet-shaped) magnetite crystals predominated in more reduced conditions in some marine sediments, leading to the idea that organic C fluxes control specific MTB populations and thus magnetite crystal morphologies (Yamazaki and Kawahata, 1998). Many or most extant MTBs are found to grow and thrive at or close to the oxic-anoxic interface (OAI) (also known as the oxic-anoxic transition zone (OATZ)), either in sediments or in water columns (Frankel *et al.* 1997; Bazylinski and Frankel 2004). Yamazaki *et al.*

(2019) reported the highest number of bullet-shaped magnetite magnetofossils at the OATZ and suggested that magnetofossil morphologies can be used to detect past OATZs. Before any established conclusions can be drawn about the use of specific magnetofossil magnetite morphologies as biomarkers, a key issue that needs to be addressed is a better understanding of the environmental conditions under which such crystals are preserved. The dissolution of magnetite is known to occur under reducing conditions in sediments (*i.e.*, in suboxic (where concentrations of dissolved O_2 and sulfide are very low) or anoxic zones below the Fe-redox boundary (Canfield and Berner, 1987; Tostevin and Poulton, 2019; Yamazaki *et al.*, 2003, 2019). Therefore, an understanding of magnetic mineral diagenesis after deposition in sediments is essential for any interpretation of magnetofossils as biomarkers. In a controlled study, Yamazaki *et al.* (2019) used a sediment core taken from the Japan Sea to study magnetosome magnetic crystal dissolution through the core. Partially etched crystals were common in the reductive dissolution zone. Interestingly, with progressive dissolution, the proportion of bullet-shaped crystals decreased while hexagonal prismatic forms became more dominant, probably due to differences in resistance to dissolution among crystal planes of magnetite and differences in surface area to volume ratio (Yamazaki *et al.*, 2019). Thus, processes of reductive diagenesis must be understood and considered when using magnetofossil morphology as a paleoenvironmental proxy. Their use as a biomarker for the present or past presence of specific groups of MTB may be less stringent. However, because several groups of MTB biomineralize bullet-shaped magnetite crystals, a knowledge of crystallographic details (such as those presented here) may provide further help in determining which groups of MTB are present.

Future developments in the magnetic characterization of magnetite in magnetosomes using TEM can include various experimental and methodological approaches. Intact magnetosome chains in their natural environment can be studied in liquid cell TEM specimen holders (Prozorov *et al.*, 2017). Information about local variations in magnetic moment within individual crystals and magnetic interactions between magnetosomes can be obtained quantitatively in three dimensions by using holographic tomography (Wolf *et al.*, 2022). The strength and direction of the magnetocrystalline anisotropy in each magnetite crystal in a chain can be probed relative to contributions from shape and magnetostatic interactions as a function of temperature, both at cryogenic and at elevated temperature around the Verwey and Curie transitions. Miniature magnetizing units built inside the objective lens area of a TEM promise to allow the use of vector magnetic fields to study magnetization rotation and reversal processes in magnetosome chains in the presence of static or rapidly varying magnetic fields, thereby providing further insight into fundamental magnetic phenomena.

In summary, quantitative magnetic imaging and measurements of the magnetic dipole moment and projected in-plane magnetization of <100>- and <110>-elongated magnetite magnetosomes from strains RS-1, LO-1 and HSMV-1 were determined using off-axis EH in the TEM. Magnetic field lines in isolated bullet-shaped magnetite magnetosomes and linear chains of crystals whose elongation directions lie along the chain axes typically follow the elongation axes of the crystals and form single magnetic domain states. However, in disordered chains, the directions of the magnetic field lines can be dominated by magnetic interactions between adjacent crystals and deviate from the elongation directions of the crystals. Quantitative analysis of our experimental results suggests that the magnetization of the studied magnetosomes may be reduced slightly from that of pure magnetite. Although our study

provides new information about the magnetic properties of <100>- and <110>-elongated magnetite magnetosomes, key information about the origin of such energetically unfavourable elongation directions remains unresolved.

References

Baumgartner J. *et al.*, (2016) Elongated magnetite nanoparticle formation from a solid ferrous precursor in a magnetotactic bacterium. *Journal of the Royal Society Interface*, **13**, 20160665.

Bazylinski D.A. and Frankel R.B., (2004). Magnetosome formation in prokaryotes. *Nature Reviews Microbiology*, **2**(3), 217–230.

Beleggia M., Kasama T. and Dunin-Borkowski R.E. (2010) The quantitative measurement of magnetic moments from phase images of nanoparticles and nanostructures-I. *Fundamentals. Ultramicroscopy*, **110**(5), 425–432.

Byrne M.E. *et al.*, (2010) Desulfovibrio magneticus RS-1 contains an iron- and phosphorus-rich organelle distinct from its bullet-shaped magnetosomes. *Proceedings of the National Academy of Sciences of the United States of America*, **107**, 12263–12268.

Canfield D.E., Berner R.A. (1987) Dissolution and pyritization of magnetite in anoxic marine sediments. *Geochim Cosmochim Acta* **51**: 645–659

Caron J. (2017) Model-based reconstruction of magnetisation distributions in nanostructures from electron optical phase images, PhD Thesis at RWTH Aachen University, vol 177.

Charilaou M., Rahn-Lee L., Kind J., García-Rubio I., Komeili A., Gehring A.U. (2015) Anisotropy of bullet-shaped magnetite nanoparticles in the magnetotactic bacteria *Desulfovibrio magneticus sp. strain RS-1*, **108**, 1268.

Charilaou M. (2017) Ferromagnetic resonance of biogenic nanoparticle-chains. *Journal of Applied Physics*, **122**, 063903.

Descamps E.C.T., Monteil C.L., Menguy N., Ginet N., Pignol D., Bazylinski D.A., Lefèvre C.T. (2017) *Desulfamplus magnetovallimortis* gen. nov., sp. nov., a magnetotactic bacterium from a brackish desert spring able to biomineralize greigite and magnetite, that represents a novel lineage in the *Desulfobacteraceae, Systematic and Applied Microbiology* **40**, 280.

Devouard B., Pósfai M., Hua X., Bazylinski D.A., Frankel R.B., Buseck P. (1998) Magnetite from magnetotactic bacteria: Size distributions and twinning. *American Mineralogist*, **83**, 1387.

Dunin-Borkowski R.E. *et al.* (1998) Magnetic microstructure of magnetotactic bacteria by electron holography. *Science*, **282**, 1868–1870.

Dunin-Borkowski R.E. *et al.*, (1998) Towards quantitative electron holography of magnetic thin films using in situ magnetization reversal. *Ultramicroscopy*, **74**, 61–73.

Dunin-Borkowski R.E. *et al.* (2001). Off-axis electron holography of magnetotactic bacteria: magnetic microstructure of strains MV-1 and MS-1. *European Journal of Mineralogy*, **13**, 671–684.

Dunin-Borkowski R.E., Kasama T., Wei A., Tripp S.L. Hÿtch M.J., Snoeck E., Harrison R.J., Putnis A. (2004). Off-axis electron holography of magnetic nanowires and chains, rings and planar arrays of magnetic nanoparticles. *Microscopy Research and Technique* **64**, 390.

Dunlop D.J. and Özdemir Ö. (1997) *Rock magnetism: Fundamentals and frontiers*. Cambridge University Press, Cambridge.

Dziuba, M. V., Müller F. D., Pósfai, M., Schüler, D. (2023) Exploring the host range for genetic transfer of magnetic nanoparticle synthesis. *Nature Nanotechnology*, 10.1038/s41565-023-01500-5

Fabian K., Kirschner A., Williams W., Heider F., Leibl T., Huber A. (1996) Three-dimensional micromagnetic calculations for magnetite using FFT. *Geophysical Journal International* **124**, 89.

Faivre D. and Schüler D. (2008) Magnetotactic bacteria and magnetosomes. *Chemical Reviews*, **108**, 4875–4898.

Frankel R.B., Bazylinski D.A., Johnson M.S. and Taylor B.L. (1997) Magneto-aerotaxis in marine coccoid bacteria. *Biophysical Journal*, **73**, 994–1000.

Goswami P., He K., Li J., Pan Y., Roberts A.P., Lin W., (2022) Magnetotactic bacteria and magnetofossils: ecology, evolution and environmental implications, *npj Biofilms and Microbioms*, **8**, 43.

Hanzlik M., Winklhofer M., Petersen N. (2002) Pulsed-field-remanence measurements on individual magnetotactic bacteria. *J. Magn. Mag. Mat.* **248**, 258.

Hertel R. and Kronmüller H. (2002) Finite element calculations on the single-domain limit of a ferromagnetic cube - a solution to μMAG Standard Problem No. 3. *Journal of Magnetism and Magnetic Materials*, **238**(2), 185–199.

Jogler C. *et al.* (2011) Conservation of proteobacterial magnetosome genes and structures in an uncultivated member of the deep-branching Nitrospira phylum. *Proceedings of the National Academy of Sciences of the United States of America*, **108**(3), 1134–1139.

Kalirai S.S., Bazylinski D.A., Hitchcock A.P. (2013) Anomalous magnetic orientations of magnetosome chains in a magnetotactic bacterium: Magnetovibrio blakemorai strain MV-1. *PLOS ONE*, **8**, e53368.

Kasama T. *et al.* (2006) Magnetic properties, microstructure, composition and morphology of greigite nanocrystals in magnetotactic bacteria from electron holography and tomography. *American Mineralogist*, **91**, 1216–1229.

Kolinko I., Jogler C., Katzmann E. and Schüler D. (2011). Frequent mutations within the genomic magnetosome island of magnetospirillum gryphiswaldense are mediated by RecA. *Journal of Bacteriology*, **193**(19), 5328–5334.

Kolinko, I. *et al.*, 2014. Biosynthesis of magnetic nanostructures in a foreign organism by transfer of bacterial magnetosome gene clusters. *Nature Nanotechnology*, **9**(3): 193–197.

Komeili A. (2012) Molecular mechanisms of compartmentalization and biomineralization in magnetotactic bacteria. *FEMS Microbiology Reviews*, **36**, 232–255.

Kopp R.E. and Kirschvink J.L. (2008) The identification and biogeochemical interpretation of fossil magnetotactic bacteria. *Earth-Science Reviews* **86**, 42.

Kovács A., Caron J., Savchenko A.S., Kiselev N.S., Shibata K., Li Z-A., Kanazawa N., Tokura Y., Blügel S., Dunin-Borkowski R.E. (2017), Mapping the magnetization fine structure of a lattice of Bloch-type skyrmions in an FeGe thin film, *Applied Physics Letters* **111**, 192410.

Kovács A., Dunin-Borkowski R.E. (2018) Handbook of Magnetic Materials, Chapter 2: Magnetic imaging of nanostructures using off-axis electron holography (E. Brück ed.), Elsevier B.V., pp 59–153.

Körnig A., Winklhofer M., Baumgartner J., Gonzalez T.P., Fratzl P., Faivre D. (2014) Magnetite crystal orientation in magnetosome chains, *Advanced Functional Materials* **24**, 3926.

Lam K.P. *et al.* (2010) Characterizing magnetism of individual magnetosomes by X-ray magnetic circular dichroism in a scanning transmission X-ray microscope. *Chemical Geology*, **270**, 110–116.

Lan Q., Kovács A., Caron J., Du H., Song D., Dasari S., Gwalani B., Chaudhary V., Ramanujan R.V., Banerjee R., Dunin-Borkowski R.E. (2022) Highly complex magnetic behavior resulting from hierarchical phase separation in AlCo(Cr)FeNi high-entropy alloys, iScience 25, 104047.

Le Sage D. *et al.* (2013) Optical magnetic imaging of living cells. *Nature*, **496**, 486–489.

Lefèvre C.T. *et al.* (2010) Moderately thermophilic magnetotactic bacteria from hot springs in Nevada. *Applied and Environmental Microbiology*, **76**, 3740–3743.

Lefèvre C.T., Frankel R.B., Abreu F., Lins U. and Bazylinski D.A., (2011a). Culture-independent characterization of a novel, uncultivated magnetotactic member of the Nitrospirae phylum. *Environmental Microbiology*, **10**, 538–549.

Lefèvre C.T. *et al.* (2011b) Morphological features of elongated-anisotropic magnetosome crystals in magnetotactic bacteria of the Nitrospirae phylum

and the Deltaproteobacteria class. *Earth and Planetary Science Letters*, **312**, 194–200.

Lefèvre C.T., Viloria N., Schmidt M.L., Pósfai M., Frankel R.B., Bazylinski D.A. (2012) Novel magnetite-producing magnetotactic bacteria belonging to the *Gammaproteobacteria*. *The ISME Journal* **6**, 440.

Lefèvre C.T. *et al.* (2013) Monophyletic origin of magnetotaxis and the first magnetosomes. *Environmental Microbiology*, **15**, 2267–2274.

Li J. *et al.* (2015) Crystal growth of bullet-shaped magnetite in magnetotactic bacteria of the Nitrospirae phylum. *Journal of the Royal Society Interface*, **12**, 20141288.

Li J. *et al.* (2010) Biomineralization, crystallography and magnetic properties of bullet-shaped magnetite magnetosomes in giant rod magnetotactic bacteria. *Earth and Planetary Science Letters*, **293**, 368–376.

Li J., Menguy N., Roberts A.P., Gu L., Leroy E., Bourgon J., Yang X., Zhao X., Liu P., Changela H.G., Pan Y. (2020) Bullet-shaped magnetite biomineralization within a magnetotactic Deltaproteobacterium: implications for magnetofossil identification. *Journal of Geophysical Research: Biogeosciences* **125**, 20.

Lin W. *et al.* (2014) Genomic insights into the uncultured genus "Candidatus Magnetobacterium" in the phylum Nitrospirae. *The ISME journal*, **8**, 2463–2477.

Lohsse [Lohße] A. *et al.* (2014) Genetic dissection of the mamAB and mms6 operons reveals a gene set essential for magnetosome biogenesis in Magnetospirillum gryphiswaldense. *Journal of Bacteriology*, **196**, 2658–2669.

Mann S., Sparks N.H.C. and Blakemore R.P. (1987) Structure, morphology and crystal growth of anisotropic magnetite crystals in magnetotactic bacteria. *Proceedings of the Royal Society of London*, **B231**, 477–487.

McCartney M.R., Lins U., Farina M., Buseck P.R. and Frankel R.B. (2001) Magnetic microstructure of bacterial magnetite by electron holography. *European Journal of Mineralogy*, **13**, 685–689.

Mériaux S., Boucher M., Marty B., Lalatonne Y., Préréval S., Motte L., Lefèvre C. T., Geffroy F., Lethimonnier F., Péan M., Garcia D., Adryanczyk-Perrier G., Pignol D., Ginet N. (2015) Magnetosomes, biogenic magnetic nanomaterials for brain molecular imaging with 17.2 T MRI scanner, *Advanced Healthcare Materials*, **4**, 1076.

Moreno R., Poyser S., Meilak D., Meo A., Jenkins S., Lazarov V.K., Vallejo-Fernandez G., Majetich S., Evans R. (2020) The role of faceting and elongation on the magnetic anisotropy of magnetite Fe$_3$O$_4$ nanocrystals 10, 2722.

Nakano S., Furutani H., Kato S., Kouduka M., Yamazaki T., Suzuki Y. (2023) Bullet-shaped magnetosomes and metagenomic-based magnetosome gene profiles in a deep-sea hydrothermal vent chimney. *Frontiers in Microbiology* **14**, 1174899.

Pohl A., Berger F., SUllan R.M.A., Valverde-Tercedor C., Freindl K., Spiridis N., Lefèvre C.T., Menguy N., Klumpp S., Blank K.G., Faivre D. (2019) *Nano Letters* **19**, 8207.

Petersen N., von Dobeneck T., Vali H. (1986) Fossil bacterial magnetite in deep-sea sediments from the South Atlantic Ocean. *Nature* **320**, 611.

Pósfai M. and Dunin-Borkowski R.E. (2009) Magnetic nanocrystals in organisms. *Elements*, **5**, 235–240.

Pósfai M., Kasama T. and Dunin-Borkowski R.E. (2013a). Biominerals at the nanoscale: transmission electron microscopy methods for studying the special properties of biominerals. In: F. Nieto and K.J.T. Livi (Editors), *Minerals at the nanoscale. EMU Notes in Mineralogy*. European Mineralogical Union and Mineralogical Society of Great Britain & Ireland, London, pp. 375–433.

Pósfai M., Lefévre C.T., Trubitsyn D., Bazylinski D.A. and Frankel R.B. (2013b). Phylogenetic significance of composition and crystal morphology of magnetosome minerals. *Frontiers in Microbiology*, **4**, 344.

Pósfai M. *et al.* (2006) Properties of intracellular magnetite crystals produced by Desulfovibrio magneticus strain RS-1. *Earth and Planetary Science Letters*, **249**, 444–455.

Proksch R. *et al.* (1995) Magnetic force microscopy of the submicron magnetic assembly in a magnetotactic bacterium. *Applied Physics Letters*, **66**, 2582–2584.

Prozorov T., Almeida T.P., Kovács A., Dunin-Borkowski R.E. (2017) Off-axis electron holography of bacterial cells and magnetic nanoparticles in liquid, *J. R. Soc. Interface* **14**, 20170464.

Rahn-Lee L. *et al.* (2015) A Genetic Strategy for Probing the Functional Diversity of Magnetosome Formation. *PLoS Genetics*, **11**, e1004811.

Sakaguchi T., Arakaki A. and Matsunaga T. (2002) Desulfovibrio magneticus sp nov., a novel sulfate-reducing bacterium that produces intracellular single-domain-sized magnetite particles. *International Journal of Systematic and Evolutionary Microbiology*, **52**, 215–221.

Saxton W.O., Pitt T.J., Horner M. (1979) Digital image processing: The SEMPER system, *Ultramicroscopy* **4**, 343.

Simpson E.T. *et al.* (2005) Magnetic induction mapping of magnetite chains in magnetotactic bacteria at room temperature and close to the Verwey transition using electron holography. *Journal of Physics: Conference Series*, **17**, 108–121.

Staniland S., Ward B., Harrison A., Van Der Laan G. and Telling N. (2007) Rapid magnetosome formation shown by real-time x-ray magnetic circular dichroism. *Proceedings of the National Academy of Sciences of the United States of America*, **104**, 19,524–19,528.

Tostevin R., Poulton S.W. (2019) *Suboxic sediments. Encyclopedia of Astrobiology*. Springer, Berlin, Heidelberg.

Uzun M., Koziaeva V., Dziuba M., Alekseeva L., Krutkina M., Sukhacheva M., Baslerov R., Grouzdev D., (2023) Recovery and genome reconstruction of novel magnetotactic *Elusimicrobiota* from bog soil, *The ISME Journal*, **17**, 204.

Wolf D., Schneider S., Rössler U.K., Kovács A., Schmidt M., Dunin-Borkowski R.E., Büchner B., Rellinghaus B., Lubk A. (2022) Unveiling the three-dimensional magnetic texture of skyrmion tubes, *Nature Nanotechnology* **17**, 250.

Yamazaki T., Kawahata H. (1998) Organic carbon flux controls the morphology of magnetofossils in marine sediments, *Geology* **26**, 1064.

Yamazaki T., Abdeldayem A.L., Ikehara K. (2003) Rock-magnetic changes with reduction diagenesis in Japan Sea sediments and preservation of geomagnetic secular variation in inclination during the last 30,000 years, *Earth, Planets and Space* **55**, 327.

Yamazaki T., Suzuki Y., Kouduka M., Kawamura N. (2019) Dependence of bacterial magnetosome morphology on chemical conditions in deep-sea sediments. *Earth and Planetary Science Letters* **513**, 135.

Zhu X., Kalirai S.S., Hitchcock A.P. and Bazylinski D.A. (2015) What is the correct Fe L$_{23}$ X-ray absorption spectrum of magnetite? *Journal of Electron Spectroscopy and Related Phenomena*, **199**, 19–26.

Zingsem B.W., Feggeler T., Terwey A., Ghaisari S., Spoddig D., Faivre D., Meckenstock R., Farle M., Winklhofer M., (2019) Biologically encoded magnonics, *Nature Communications* **10**, 4345.